# Thickness-dependent photovoltaic effect in monocrystalline lithium niobate films of nanoscale thickness

Yuchen Zhang, Sanbing Li, Yuejian Jiao, Xiaojie Wang, Feng Gao, Fang Bo, Jingjun Xu, and Guoquan Zhang*

*The MOE Key Laboratory of Weak-Light Nonlinear Photonics, School of Physics and TEDA Applied Physics Institute, Nankai University, Tianjin 300071, China*

(Received 15 November 2023; revised 8 February 2024; accepted 9 April 2024; published 3 May 2024)

We report that the photovoltaic (PV) effect in nanoscale monocrystalline lithium niobate (LN) films originates from the Schottky barrier formed at the electrode-LN interface, different from the bulk PV effect reported previously in the bulk crystal. The Schottky barrier height and the depletion layer width at the Cr-LN interface was measured to be 1.15 eV and 16 nm, respectively. The open-circuit voltage and the power conversion efficiency of the PV devices based on LN films were determined to be 0.8 V and 0.1%, respectively, at 325 nm. It was found the PV properties are film-thickness-dependent, mainly due to the increasing contribution of the polarization-induced asymmetric conduction from the bulk layer with the increase of LN film thickness. Furthermore, direct tunneling of electrons was observed to become the dominant conduction mechanism in ultrathin LN films (much less than 16 nm). These results could be useful for developing integrated optoelectronic devices, such as PV devices and photodetectors based on LN films.

DOI: 10.1103/PhysRevApplied.21.054009

## I. INTRODUCTION

Ferroelectrics, as a competitive material candidate for photovoltaic (PV) devices, has attracted much attention due to its intrinsic asymmetric potential and being free from the Shockley-Queisser limit [1]. In the early 1950s, the PV effect was detected in ferroelectrics [2], manifested as the generation of a steady photocurrent in a uniform crystal under a homogeneous illumination, and was explained as being due to the noncentrosymmetric lattice potential-induced asymmetric momentum distribution of the photogenerated charge carriers [3]. In order to distinguish it from the traditional PV effect, it was named as the anomalous PV effect or bulk PV effect (BPVE). In addition, the strengthened depolarization field ($E_{dp}$) in ferroelectric thin film [4], the potential step at the domain wall [5], or the Schottky barrier arising from the band alignment at the contact interface [6] can also induce an effective space-charge field to separate the photogenerated charge carriers. In recent decades, many stirring breakthroughs have been discovered in ferroelectric PV devices, including above-band-gap photovoltage [5], switchable photoresponse [7,8], and tuned low-band-gap ferroelectrics with high PV conversion efficiency [9,10]. In consequence, promising applications such as nonvolatile memory [11,12], solar-energy harvester [13], self-powered photodetector [14,15], and reconfigurable photosensor [16] were demonstrated.

Lithium niobate (LN), an excellent uniaxial ferroelectric material with a large spontaneous polarization $\mathbf{P}_s$ along the crystalline $c$ axis at temperature below the Curie temperature ($T_c \approx 1210°C$) [17], is of large nonlinear optical ($d_{33} = 25.2$ pm/V) [18] and electro-optic coefficients ($r_{33} = 30.8$ pm/V) [19], which ensure that LN is an excellent material platform for nonlinear optical and electro-optic applications. The BPVE in LN was observed in the 1960s [20], and was found to be enhanced greatly in iron-doped LN [21,22]. Nevertheless, suffering from its large band gap (approximately 4.0 eV) [23], and the associated low mobility, short lifetime, and short diffusion length of the photogenerated charge carriers, the energy conversion efficiency is extremely low, usually in the range of $10^{-6}$–$10^{-4}$. With the advancement of thin-film fabrication techniques, the photocurrent density of iron-doped LN thin films with a preferred $c$-axis orientation, prepared using pulsed-laser deposition, has shown a 500-fold enhancement as compared to that of the bulk crystal obtained by Festl *et al.* [22,24]. In fact, it reached 50 $\mu A/cm^2$ under an 1-$W/cm^2$ illumination (photon energy 3.11 eV) [24]. Recently, the successful preparation of monocrystalline LN thin film by crystal-ion-slicing technology opens up the exploration of LN at the nanoscale thickness and forges ahead for the development of optoelectronics, yielding domain or domain-wall-based memristor [25,26],

*Corresponding author: zhanggq@nankai.edu.cn

 

domain-wall *p*-*n* junction [27], vibrational energy harvester [28], and high-sensitive photodetector [29,30].

## II. RESULTS AND DISCUSSIONS

The PV effect of monocrystalline nanoscale LN films was studied under the illumination of light at 325 nm. The structure of the PV device was composed of a *z*-cut nominally pure congruent monocrystalline LN thin film (the top surface was the $+z$ surface), a 100-nm Cr layer serving as the bottom electrode, a 2-μm silica layer, and a 500-μm LN substrate that were bonded one another in sequence, as shown schematically in Fig. 1(a). The PV devices with different LN film thickness were prepared by polishing the top 100-nm LN film down to the desired film thickness using chemical-mechanical polishing (CMP) technique. To study the PV effect, an additional Cr electrode was deposited on the top surface of the LN film. More details about the device fabrication and characterization can be found in Appendix A. Figure 1(b) illustrates the dependence of the absolute value of the short-circuit current density ($J_{sc}$) and the open-circuit voltage ($V_{oc}$) on the LN film thickness $d$. Here we defined the current density $J_{sc}$ to be positive when the current flows from the top electrode to the bottom electrode in the PV devices. The power density of the incident light $P_{in}$ on the top surface of the LN film was 135 mW/cm$^2$. One sees that, as the LN film thickness decreases, $|J_{sc}|$ increases rapidly up to a maximum of 0.377 mA/cm$^2$ at around $d = 16$ nm, then followed by a sharp decrease. It was also found that $J_{sc}$ is parallel to the polarization $\mathbf{P}_s$ of the LN film, which is very different from that of the BPVE observed in bulk LN crystals where the PV current is antiparallel to the spontaneous polarization $\mathbf{P}_s$ [20]. On the other hand, with the decrease of $d$, $V_{oc}$ remains at approximately 0.8 V at first and then decreases sharply when $d$ is less than 16 nm. This is also very different from the BPVE, indicating that the BPVE is not the underlying mechanism for the observed PV effect in our devices. In fact, it was experimentally measured that the field induced by BPVE in LN is only around 500 V/cm when the excitation wavelength is in the ultraviolet [31], therefore, one can estimate that the PV voltage induced by BPVE is approximately $8.0 \times 10^{-4}$ V for a 16-nm LN film, which is 3 orders of magnitude smaller than the observed PV voltage of 0.8 V in our LN films, indicating that the contribution from the BPVE is negligible.

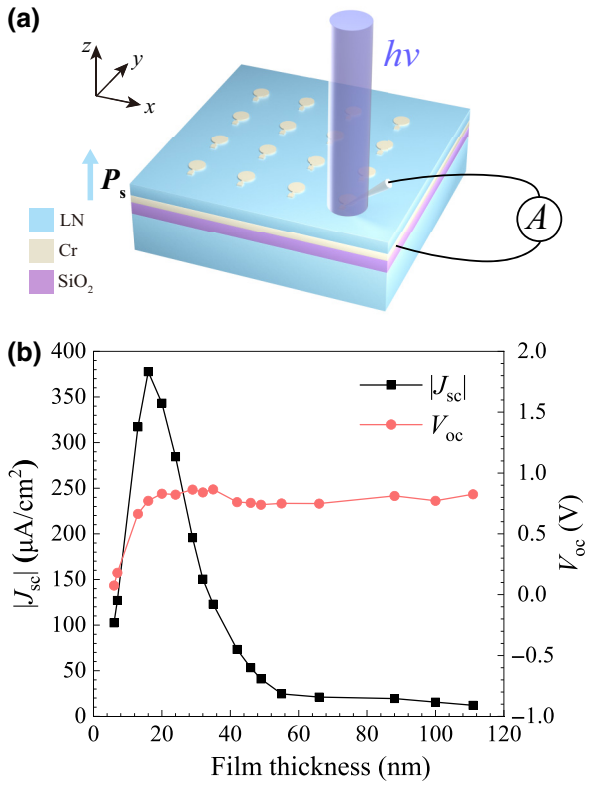


FIG. 1. (a) Schematic structure of the PV device. (b) The dependence of $|J_{sc}|$ and $V_{oc}$ on the LN film thickness $d$. The curves are guided by eyes.

We also studied the dependence of the photoinduced current density $J$ on the externally applied voltage $V$, i.e., the $J$-$V$ curves of the PV devices of different LN film thickness. Typical results are shown in Fig. 2 under an illumination of light at 325 nm of 135 mW/cm$^2$ and with $d$ larger than 16 nm (the results for the cases with $d$ less than 16 nm will be discussed separately in the following). One sees that two different behaviors of the $J$-$V$ curves were observed, one is J shaped and the other is S shaped, as shown in Figs. 2(a) and 2(b), respectively. With the increase of $d$, the J-shaped $J$-$V$ curves were transferred to the S-shaped ones. Note that the PV response due to BPVE is usually dependent on the light polarization, as those observed in $BiFeO_3$ [32]. While in our configuration the PV response is independent of the light polarization, which also indicates that the contribution from the BPVE is negligible.

The nominally congruent LN is an *n*-type ferroelectrics with electrons being the majority carriers. The electron affinity of LN was reported to be 1.5 eV [33], and the work function of LN is lower than that of Cr (4.5 eV) [34], therefore a band bending may occur at the Cr-LN interfaces, leading to a Schottky barrier, which can induce a build-in field ($E_{bi}$) in the depletion region. The build-in field $E_{bi}$ will separate photogenerated electron-hole pairs, resulting in the PV current [35]. To confirm the existence of the Schottky barrier, we measured the $J$-$V$ curves in dark (see Appendix B), which shows a diodelike behavior resembling a single *p*-*n* junction, indicating the presence of a Schottky contact at the top Cr-LN interface and a flattened energy-band alignment at the bottom LN-Cr interface. This is feasible because of the polarization-dependent interface properties of LN, such as compensating charge polarity, interface states, and surface electron affinity [33,35,36], which may lead to an increase in the band bending at

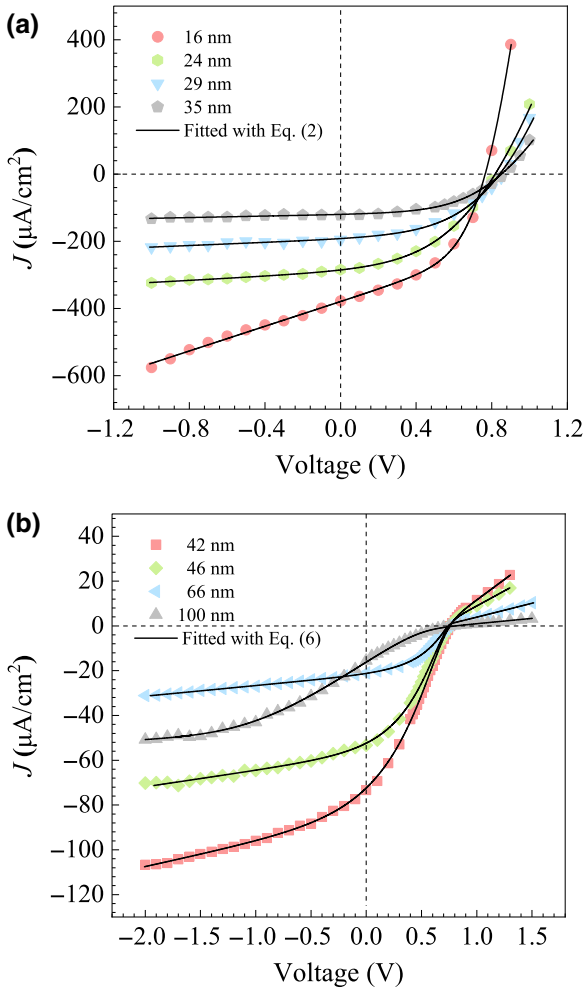


FIG. 2. The $J$-$V$ curves of the PV devices with different LN film thickness. (a) Cases with LN film thicknesses of 16, 24, 29, and 35 nm, respectively. All $J$-$V$ curves are J shaped. (b) Cases with LN film thicknesses of 42, 46, 66, and 100 nm, respectively. All $J$-$V$ curves are S shaped. In all cases, the power density $P_{in}$ incident on the top LN film was 135 mW/cm$^2$ at 325 nm. The solid curves are the theoretical fits using Eq. (2) for (a) and Eq. (6) for (b), respectively.

the $+z$ interface and a decrease in that at the $-z$ interface [37]. Besides, the fabrication process of the electrodes can also influence the barrier height, even if they are made from the same material [38]. One notes that, in most cases, the higher Schottky barrier is usually formed at the tail of the spontaneous polarization $\mathbf{P}_s$ in $BiFeO_3$ and $Pb(Zr_{0.2}Ti_{0.8})O_3$ (PZT) [6,39,40]. Occasionally, there are also reports that the higher Schottky barrier forms at the head of the ferroelectric polarization $\mathbf{P}_s$ in $BiFeO_3$, PZT, $Bi_{0.9}La_{0.1}FeO_3$, and so on [41–43]. This is probably due to the different surface defect states and different screening mechanism between LN and $BiFeO_3$ and PZT [44,45]. The Schottky emission conduction mechanism of the devices was further confirmed by the temperature-dependent $J$-$V$ characteristics in dark (see Appendix B), which can be well described by the Schottky-Simmons equation [46], and the Schottky barrier height at the top Cr-LN interface was estimated to be approximately 1.15 eV. Accordingly, Fig. 3(a) depicts the schematic band diagram of our PV devices when the LN film thickness $d$ is larger than the depletion layer width $w$ at the top Cr-LN interface, where the build-in field $E_{bi}$ is pointing towards the top Cr electrode, leading to a PV current parallel to the polarization $\mathbf{P}_s$ of the LN film.

In the case when the LN film thickness $d$ is close to (but larger than) the depletion layer width $w$, the $J$-$V$ characteristics is mainly determined by the Schottky barrier, and the effect due to the recombination and trapping process in the bulk layer is negligible. The equivalent circuit, consisting of an ideal diode $D_1$, a constant photoinduced current source $J_{ph}$, a series resistance $R_s$, and a shunt resistance $R_{sh}$, is illustrated in Fig. 3(b). It is generally accepted that $R_s$ primarily stems from the contact resistance and the bulk resistance introduced in the devices. On the other hand, $R_{sh}$ reflects the extent of current loss attributed to the recombination and trapping of charge carriers mainly in the depletion layer [47,48]. Based on the Schottky equation [35], the $J$-$V$ relationship can be described as

$$J = J_{01}\left(e^{\frac{q(V-JR_sA)}{n_1k_BT}} - 1\right) + \frac{V - JR_sA}{R_{sh}A} - J_{ph}, \quad (1)$$

where $J_{01}$ is the reverse saturation current density, $q$ is the elementary charge, $n_1$ is the ideality factor, $k_B$ is the Boltzmann constant, $T$ is the temperature in kelvins, and $A$ is the electrode area. Equation (1) can be solved by employing the Lambert $W$ function [49], giving

$$V = \left(JR_s + \left(J + J_{ph} + J_{01}\right)R_{sh}\right)A - \frac{n_1k_BT}{q}W\left(\frac{qJ_{01}R_{sh}A}{n_1k_BT}e^{\frac{q\left(J+J_{ph}+J_{01}\right)R_{sh}A}{n_1k_BT}}\right). \quad (2)$$

The solid curves in Fig. 2(a) are the fitted ones using Eq. (2), which are in good agreement with the experimental data, affirming the validity of the proposed model [46].

With the increase of the LN film thickness $d$, one has to take the effect of the bulk layer into consideration, and the PV effect of the devices is the result of a combination of a Schottky diode and a bulk layer. One notes that the open-circuit voltage $V_{oc}$ is thickness independent, indicating the BPVE is negligible. On the other hand, the presence of the polarization $\mathbf{P}_s$ in the bulk layer would establish an asymmetric potential barrier, which favors the movement of electrons towards the $+z$ surface of the LN film. Therefore, the charge-carrier transport in the bulk layer is asymmetric, akin to a diode but operating in the opposite direction with respect to the Schottky diode in the depletion layer. Accordingly, the equivalent circuit of the PV devices is

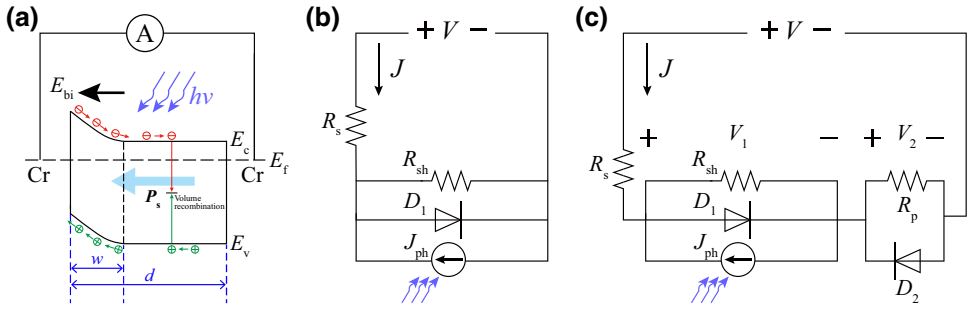


FIG. 3. Physical models of the PV effect in the cases with $d \sim w$ or $d > w$. (a) Schematic band diagram of the PV devices based on the Schottky barrier model. The red and green arrows represent the transport direction of the photogenerated electrons and holes, respectively, driven by the build-in field $E_{bi}$. The processes of volume recombination and trapping of the photogenerated charge carriers in the bulk layer are illustrated. $E_f$, $E_c$, and $E_v$ represent the Fermi level, the conduction band, and the valence band of LN. (b),(c) The equivalent circuits exhibiting the J-shaped and the S-shaped $J$-$V$ curves, respectively.

shown in Fig. 3(c), where the charge-carrier transport in the bulk layer is mimicked by a diode $D_2$ connected in parallel with a resistance $R_p$ representing the blocking effect induced by the charge-carrier loss due to the recombination and trapping in the bulk layer. Therefore, the terminal voltage of the circuit is given by

$$V = V_1 + V_2, \tag{3}$$

with $V_1$ and $V_2$ being acquired from the following equations:

$$J = J_{01}\left(e^{\frac{q(V_1 - JR_sA)}{n_1 k_B T}} - 1\right) + \frac{V_1 - JR_sA}{R_{sh}A} - J_{ph}, \tag{4}$$

$$J = -J_{02}\left(e^{-\frac{qV_2}{n_2 k_B T}} - 1\right) + \frac{V_2}{R_pA}, \tag{5}$$

where $J_{0i}$ and $n_i$ are the reverse saturation current density and the ideality factor of diode $D_i$ ($i = 1$ or 2), respectively. Similarly, Eqs. (4) and (5) can be solved by employing the Lambert $W$ function, giving

$$\begin{aligned} V = {} & \left(JR_s + \left(J + J_{ph} + J_{01}\right)R_{sh} + \left(J - J_{02}\right)R_p\right)A \\ & - \frac{n_1 k_B T}{q} W\left(\frac{qJ_{01}R_{sh}A}{n_1 k_B T} e^{\frac{q\left(J + J_{ph} + J_{01}\right)R_{sh}A}{n_1 k_B T}}\right) \\ & + \frac{n_2 k_B T}{q} W\left(\frac{qJ_{02}R_pA}{n_2 k_B T} e^{\frac{q\left(J_{02} - J\right)R_pA}{n_2 k_B T}}\right). \end{aligned} \tag{6}$$

The fitted curves exhibit a good agreement with the experimental data, as demonstrated by the solid curves in Fig. 2(b).

Also, one can extract parameters such as parasitic resistances $R_s$, $R_{sh}$, and $R_p$ based on the proposed model. The dependence of these parameters on the LN film thickness is shown in Fig. 4(a). One sees that both $R_{sh}$ and $R_p$ increase monotonically with the increase of $d$, while $R_s$ becomes more pronounced in devices with thicker LN films. By applying a linear fit to $R_p$, the intersection point with the horizontal axis is estimated at 36 nm [see Fig. 4(a)]. This proves that, when $d$ is less than 36 nm, the photogenerated charge carriers in the depletion layer can be collected efficiently by the Cr electrodes, indicating that the blocking effect on the drift carrier in the bulk layer is negligible. Therefore, the equivalent circuit is effectively simplified from Figs. 3(c) to 3(b), and the S-shaped $J$-$V$ curves are transferred to the J-shaped ones with the decrease of $d$, as confirmed by the experimental results in Fig. 2. These results offer valuable insights into the influence of parasitic resistances on the overall PV performance and highlight the impact of the LN film thickness on the PV performance of our devices.

Figures 4(b) and 4(c) depict the dependence of $|J_{sc}|$ and $V_{oc}$ on the incident power density $P_{in}$ for devices featuring three typical LN film thicknesses. The corresponding $J$-$V$ curves are shown in Appendix C. As expected, the $|J_{sc}|$ increases with increasing $P_{in}$, following a power-law relationship $|J_{sc}| \propto P_{in}^{\alpha}$ [50]. Here, the power exponent $\alpha$ decreases with the increase of $d$ and varies within [0, 1]. In the case with a LN film thickness comparable to or less than the depletion width of the Schottky barrier, the series resistance $R_s$ is small, and the photogenerated charge carriers are collected efficiently by the electrodes, then the short-circuit current $J_{sc}$ is proportional to the photoinduced current $J_{ph}$ according to Eq. (1), therefore, is proportional to the incident light power density $P_{in}$, and $\alpha$ will approach to unity. With the increase of LN film thickness, the photogenerated charge carriers are not fully collected by the electrodes due to the recombination and trapping processes in the bulk layer [51,52], therefore the charge-collection efficiency decreases, and the resistances $R_s$, $R_p$, and $R_{sh}$ increase, as shown in Fig. 4(b), leading to the decrease of $\alpha$. Note that contributions from BPVE could be negligible in our case. Similar behavior was also observed

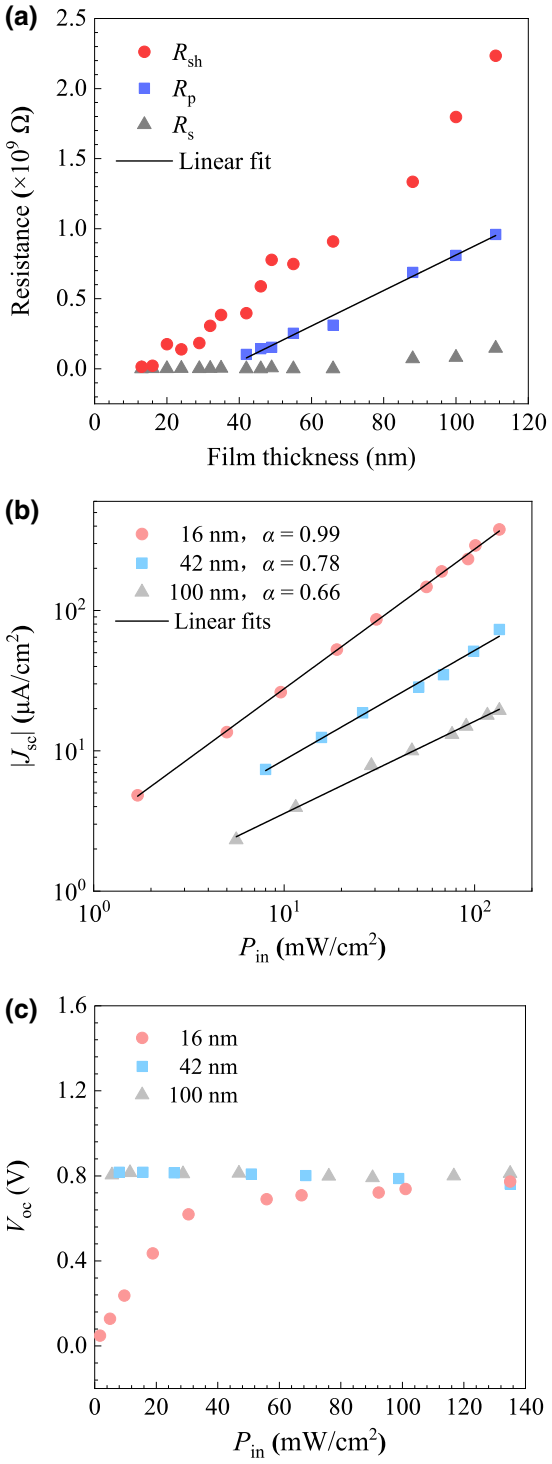


FIG. 4. (a) Parasitic resistances $R_s$, $R_{sh}$, and $R_p$ as a function of the LN film thickness $d$. (b),(c) The dependence of $|J_{sc}|$ and $V_{oc}$, respectively, on the power density $P_{in}$ for three typical devices with $d = 16$, 42, and 100 nm. The lines in (a),(b) are the linear fits to the experimental data.

in other heterojunction devices and following the same power law [50,51,53,54]. On the other hand, $V_{oc}$ increases with increasing $P_{in}$ due to the increase of the photoinduced current $J_{ph}$ but finally tends to be saturated at the build-in Schottky potential for the cases with thinner LN films, according to Eq. (1). However, for the cases with thicker LN film and under open-circuit condition, the photogenerated charge carriers are mainly consumed in the bulk layer through recombination and trapping at the defect centers, therefore, $V_{oc}$ is mainly determined by the build-in Schottky potential and is almost independent of $P_{in}$, as shown in Fig. 4(c).

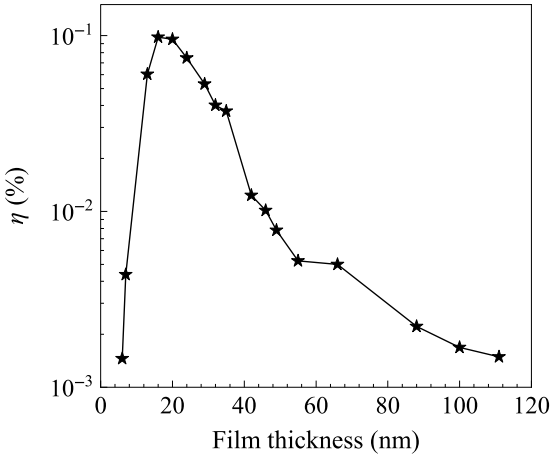


FIG. 5. The dependence of the power-conversion efficiency $\eta$ on the LN film thickness $d$ with $P_{in} = 135$ mW/cm$^2$ at 325 nm.

A crucial criterion in evaluating the potential of a material for PV devices is the power-conversion efficiency $\eta$, which is calculated as $\eta = (J \times V)_{max}/P_{in}$. The dependence of $\eta$ on the LN film thickness $d$ is shown in Fig. 5. One sees that, with the decrease of $d$, the power conversion efficiency $\eta$ increases first up to a maximum of 0.1% at $d = 16$ nm and then drops quickly. It is known that, for PV devices based on the Schottky effect, $\eta$ is maximized when the film is fully depleted and the photogenerated charge carriers are collected efficiently by the electrodes. Therefore, the depletion-layer width $w$ at the top Cr-LN interface can be estimated to be approximately 16 nm. Although $\eta$ of our PV devices is not ideal at present (see Table I in Appendix D), various strategies, such as doping [55–57], introducing semiconductor layers [58–60], adjusting dielectric film thickness [6,61,62], and altering electrode materials [63], could be explored to improve $\eta$.

Interestingly, for the PV devices with an ultrathin LN film much less than the depletion-layer width $w$, the $J$-$V$ curves were found to be symmetric and increased almost linearly, no matter for the dark and the light illuminated cases, as typically shown in Fig. 6(a) with $d = 6$ nm. The differential conductance $dI/dV$ in dark shows a parabolic characteristics [see Fig. 6(b)], which is a clear signature of direct tunneling of charge carriers through the Schottky barriers as the dominant conduction mechanism [64–67].

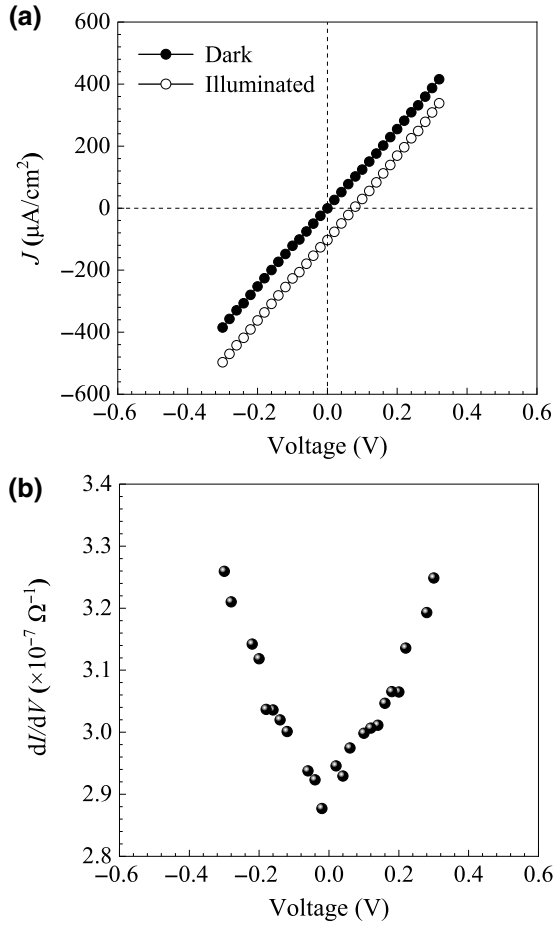


FIG. 6. (a) The $J$-$V$ curves of the PV device with an ultrathin LN film in dark and under the light illumination of 135 mW/cm$^2$ at 325 nm. (b) The differential conductance of the PV device in dark. The LN film thickness was 6 nm in all cases.

Note that, due to the negligible BPVE in our case, the contribution from the ballistic or shift conduction like those in $BiFeO_3$ and $CuInP_2S_6$ [68,69] may be negligible.

## III. CONCLUSIONS

In conclusion, we studied the PV effect of monocrystalline LN thin films with nanoscale thickness. It is found that the PV effect of the monocrystalline LN thin films is mainly originated from the Schottky barrier formed at the Cr-LN interface, which is totally different from the BPVE previously found in the bulk LN crystals. The Schottky barrier height is approximately 1.15 eV and an associated build-in field $E_{bi}$ separates the photogenerated charge carriers, generating a steady-state PV current. The depletion-layer width of the Schottky barrier is about 16 nm and the $J$-$V$ curves are typically J shaped when the LN film thickness is close to the depletion-layer width so that the conduction contribution from the bulk layer is negligible. With the increase of the LN film thickness, the asymmetric charge-carrier transport in the bulk layer due to the presence of the polarization $\mathbf{P}_s$ should be taken into account, and the $J$-$V$ curves are transferred to the S-shaped ones. The open-circuit voltage and the power conversion efficiency were measured to be 0.8 V and approximately 0.1%, respectively, which could be potentially improved further on. Interestingly, when the LN film thickness is much less than the depletion-layer width, direct tunneling of electrons becomes the dominant conduction mechanism. These results should be useful for design and optimization of integrated optoelectronic devices, such as PV devices and photodetectors based on LN films.

## ACKNOWLEDGMENTS

This work is supported by the National Key Research and Development Program of China (Grants No. 2022YFA1404604, No. 2019YFA0705000), the National Natural Science Foundation of China (NSFC) (Grant No. 12134007), the Tianjin Municipal Natural Science Foundation (Grant No. 21JCZDJC00150), and the 111 project (B23045).

## APPENDIX A: DEVICE FABRICATION AND CHARACTERIZATION

The pristine 3-in. sample used in our experiments had a layered structure composed of a 100-nm $z$-cut nominally pure congruent monocrystalline LN thin film (the top surface was the $+z$ surface), a 100-nm Cr layer serving as the bottom electrode, a 2-μm silica layer, and a 500-μm LN substrate that were bonded one another in sequence, and it was sliced into pieces, each with an area of 5 × 5 mm$^2$ (commercially provided by NANOLN, Jinan, China). The LN films with different thicknesses were prepared by employing chemical-mechanical polishing (CMP) technique to mill the pristine films with different polishing time while keeping other parameters, such as the mechanical pressure on the pristine films, the concentration of the polishing solution (MasterMet, available from Buehler), and the rotation speed (30 rpm), the same. Prior to film characterization and device fabrication, all films were cleaned in the piranha solution (7:3 98% $H_2SO_4$:30% $H_2O_2$) at 75°C for 2 min, rinsed with distilled water, and finally dried in a stream of nitrogen.

The surface topography of the CMP-milled thin films was examined in both two dimensions (2D) and three dimensions (3D) by AFM in a contact mode, as shown in Figs. 7(a) and 7(b), and the surface roughness was measured to be 0.3 nm. The thickness of the LN films could be extracted from the cross-section images measured with SEM for relatively thick films or TEM for ultrathin films. Typical results are shown in Fig. 8, where the LN film thicknesses were measured to be 100 and 66 nm for cases in Figs. 8(a) and 8(b), respectively, based on the SEM images, and 16 and 6 nm for cases in Figs. 8(c) and 8(d), respectively, based on the TEM images.

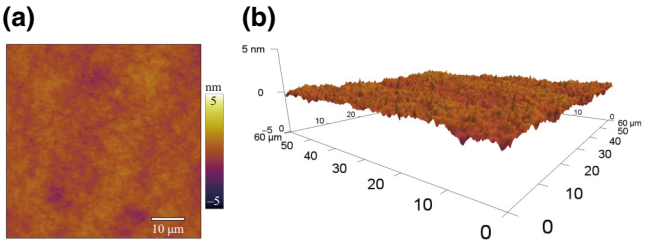


FIG. 7. The 2D (a) and 3D (b) surface topography of the CMP-milled LN thin films measured by AFM.

For characterization of the PV performance of the LN films, a semitransparent Cr electrode with a thickness of 70 nm was deposited at room temperature on the top $+z$ surface of the LN film by means of the UV photolithography, magnetron sputtering, and lift-off technique. A typical top Cr electrode was composed of a circular Cr film with a radius of 80 μm and a square Cr film with a side length of 50 μm, which were connected by a rectangular Cr film with a length of 17 μm and a width of 32 μm. A 325-nm linearly polarized He-Cd laser beam (KIMMON IK3301R-G) was expanded by a beam expander, and then passed through an adjustable attenuator (AA), a small pinhole and a mirror in succession, and was finally launched normally onto the top surface of the sample with a beam radius of 375 μm. The power of the incident light was adjusted by AA and was measured with an optical power meter, and then the light power density was calculated by dividing the measured light power over the beam spot area. The transmittance of the top Cr electrode was measured to be 17% at 325 nm. By multiplying the transmittance of the top Cr electrode, the light power density $P_{in}$ transmitted through the top Cr electrode and launched onto the underneath LN film was obtained. For most measurements in this paper, the light power density $P_{in}$ was set to be 135 mW/cm$^2$ except for those specifically pointed out, for example, in the case when studying the $P_{in}$ dependence of the $J$-$V$ characteristics.

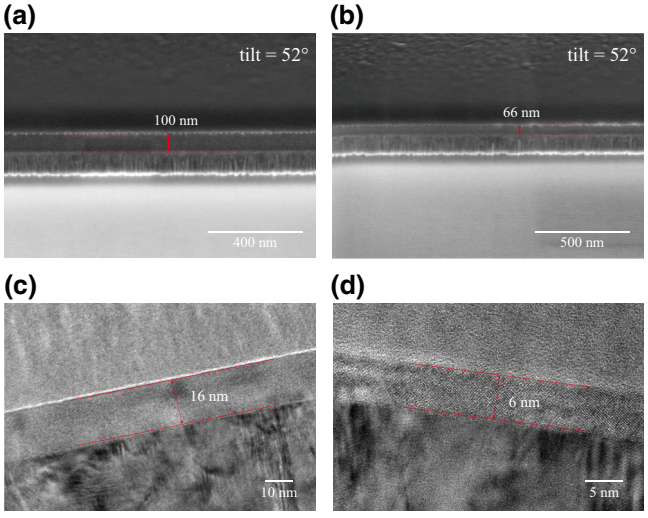


FIG. 8. Cross-section SEM images [(a),(b)] and TEM images [(c),(d)] of the device structure, from which the LN film thicknesses were determined to be 100 nm (a), 66 nm (b), 16 nm (c), and 6 nm (d), respectively.

During the measurement, the top Cr electrode was connected to a voltage source provided by a Keithley ammeter (Keithley 6517B) using a probe head equipped with a flexible tungsten needle (GGB Industries, T-4-35), while the bottom Cr electrode was connected to the ammeter through a probe head equipped with a hard tungsten needle (GGB Industries, ST-20-10), which was then drawn out with conductive silver paste and grounded. With this configuration, the $J$-$V$ characteristics were measured, and the current density was defined as positive when it flows from the top electrode to the bottom electrode, and vice versa. Moreover, all experiments were performed at room temperature (298 K, except for the temperature-dependent experiments) and under the same ambient conditions.

## APPENDIX B: TEMPERATURE-DEPENDENT $J$-$V$ CHARACTERISTICS IN DARK

In materials with low charge-carrier mobility, the characteristics of the leakage current are typically analyzed in the frame of the interface-controlled and bulk-limited Schottky-Simmons emission [46]. The forward-bias current of the Schottky barrier typically exhibits a temperature-dependent behavior as follows [35,46]:

$$J \sim 2q\left(\frac{2\pi m_{\mathrm{eff}} k_{\mathrm{B}} T}{h^2}\right)^{\frac{3}{2}} \mu E e^{-\frac{q\varphi_{\mathrm{B0}}}{k_{\mathrm{B}} T}}\left(e^{\frac{qV}{nk_{\mathrm{B}} T}} - 1\right). \quad \text{(B1)}$$

Here, $q$ is the elementary charge, $m_{\mathrm{eff}}$ is the effective mass, $k_{\mathrm{B}}$ is the Boltzmann constant, $T$ is the temperature in kelvins, $h$ is the Planck constant, $\mu$ is the charge-carrier mobility in LN, $E$ is the electric field, $q\varphi_{\mathrm{B0}}$ is the barrier height at zero bias, and $n$ is the ideality factor. Note that the associated parasitic resistances $R_{\mathrm{s}}$, $R_{\mathrm{sh}}$, and $R_{\mathrm{p}}$ are all omitted in Eq. (B1) for simplicity. This is justified by the fact that $R_{\mathrm{s}}$ and $R_{\mathrm{p}}$ are relatively small, while $R_{\mathrm{sh}}$ is large in dark, and therefore they do not affect significantly the overall trend of the Schottky-Simmons emission.

At a fixed voltage and under the condition that $e^{(qV/nk_BT)} \gg 1$, Eq. (B1) is modified as

$$\ln\left(\frac{J}{T^{\frac{3}{2}}}\right) \sim \ln\left(2q\left(\frac{2\pi m_{\mathrm{eff}} k_{\mathrm{B}}}{h^2}\right)^{\frac{3}{2}} \mu E\right) - \frac{q\varphi_{\mathrm{app}}}{k_{\mathrm{B}} T}, \quad \text{(B2)}$$

where $\varphi_{\mathrm{app}}$ is the apparent potential barrier and can be expressed as

$$\varphi_{\mathrm{app}} = \varphi_{\mathrm{B0}} - \frac{V}{n}. \quad \text{(B3)}$$

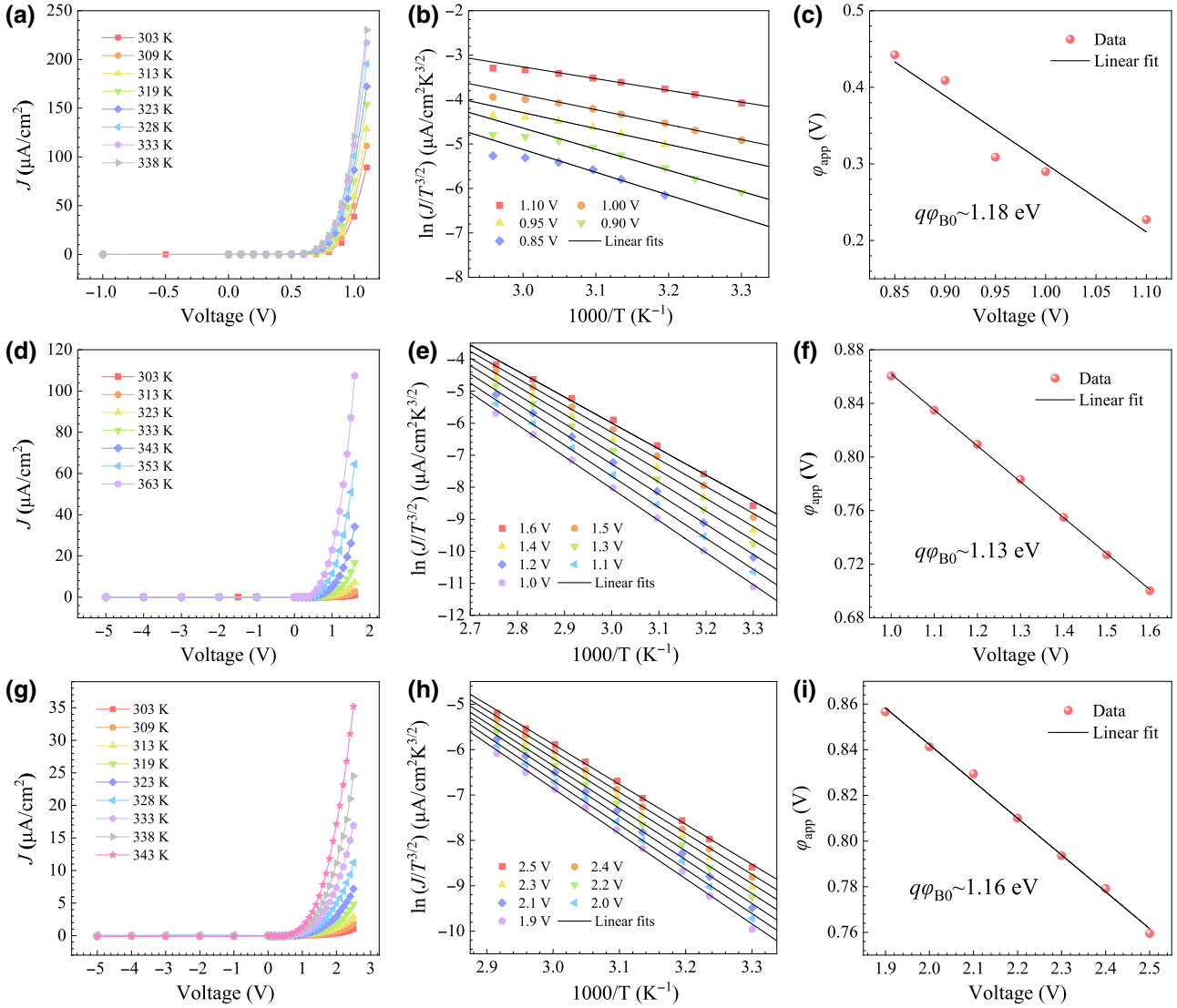


FIG. 9. (a),(d),(g) The $J$-$V$ characteristics of the PV devices in dark with different LN film thicknesses $d$ at different temperatures. (b),(e),(h) The plots of $\ln(J/T^{3/2}) \sim 1/T$ applied with different voltages and their linear fits based on Eq. (B2) with different LN film thickness. (c),(f),(i) The $\varphi_{app} \sim V$ dependence and their linear fits based on Eq. (B3) with different LN film thickness. The results in the first (a)–(c), second (d)–(f), and third (g)–(i) rows are for the PV devices with different LN film thickness of 35, 49, and 88 nm, respectively.

According to Eq. (B2), the plot of $\ln(J/T^{3/2}) \sim 1/T$ should be a straight line at a given voltage, allowing for the estimation of $\varphi_{app}$ from its slope. Then, based on Eq. (B3), $\varphi_{app}$ should have a linear relationship on $V$, with the intercept on the vertical axis providing the value of $\varphi_{B0}$.

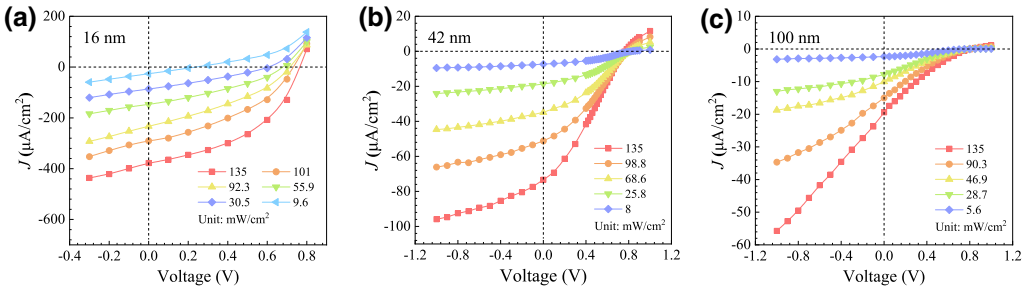


FIG. 10. The $J$-$V$ characteristics under the 325-nm light illumination with various $P_{in}$ for devices with different LN film thickness of 16 (a), 42 (b), and 100 nm (c), respectively.

TABLE I. Summary of PV performances with various materials and structures. λ, incident light wavelength; *d*, ferroelectric-dielectric layer thickness. FTO, fluorine-doped tin oxide; SRO, $SrRuO_3$; BFO, $BiFeO_3$; BCaFO, $Bi_{0.8}Ca_{0.2}FeO_{3-\delta}$; BCaFTiO, $Bi_{0.8}Ca_{0.2}Fe_{0.8}Ti_{0.2}O_{3-\delta}$; BFTO, $Bi_5FeTi_3O_{15}$; NSTO, Nb-doped $SrTiO_3$; ITO, indium tin oxide; PZT, $Pb(Zr, Ti)O_3$; BTO, $BaTiO_3$; AM 1.5G, air mass 1.5 global illumination. ⋆, This work.

| Device structure | λ (nm) | $P_{in}$ (mW/cm$^2$) | *d* (nm) | $J_{sc}$ (mA/cm$^2$) | $V_{oc}$ (V) | η (%) | Refs. |
|---|---|---|---|---|---|---|---|
| FTO/BFO/Au | AM 1.5G | 100 | 500 | $3 \times 10^{-4}$ | $0.35 \sim 3$ | $5 \times 10^{-4}$ | [56] |
| FTO/BCaFO/Au | | | | 3.2 | 0.3 | 0.22 | |
| FTO/BCaFTiO/Au | | | | 0.4 | 0.5 | 0.12 | |
| Ag/BFTO/NSTO | 405 | 200 | 200 | $4.5 \times 10^{-2}$ | 0.46 | $3 \times 10^{-3}$ | [59] |
| Ag/ZnO/BFTO/NSTO | | | 100/200 | 2.2 | 0.15 | 0.045 | |
| ITO/PZT/Pt | AM 1.5G | 100 | 270 | $4 \times 10^{-2}$ | 0.56 | $8 \times 10^{-3}$ | [58] |
| ITO/PZT/$Cu_2O$/Pt | | | 270/150 | 4.8 | 0.42 | 0.57 | |
| Pt/PZT/SRO | 365 | 170 | 300 | 0.69 | 0.91 | 0.13 | [6] |
| | | | 180 | 1.55 | 0.91 | 0.28 | |
| | | | 120 | 2.28 | 0.9 | 0.51 | |
| | | 22.3 | 12 | 1.94 | 0.84 | 2.49 | |
| Pt/BTO/Pt | 360 | 750 | 50 | $7.5 \times 10^{-3}$ | 0.65 | ... | [61] |
| | | | 20 | $4.5 \times 10^{-3}$ | 0.6 | ... | |
| ITO/PZT/Pt | AM 1.5G | 100 | 300 | 0.11 | 0.67 | 0.027 | [63] |
| ITO/PZT/Au | | | | 0.29 | 0.76 | 0.075 | |
| ITO/PZT/Ag | | | | 1.34 | 0.82 | 0.42 | |
| Cr/LN/Cr | 325 | 135 | 16 | 0.377 | 0.8 | 0.1 | ⋆ |

Here, we measured the *J*-*V* curves in dark for devices with different LN film thickness of 35, 49, and 88 nm, as shown in Figs. 9(a), 9(d) and 9(g), respectively, at various temperatures. The plots of $\ln(J/T^{3/2}) \sim 1/T$ with different voltages are presented in Figs. 9(b), 9(e), and 9(h), together with their linear fits based on Eq. (B2). The $\varphi_{app} \sim V$ dependence and their linear fits according to Eq. (B3) are shown in Figs. 9(c), 9(f), and 9(i), and from the intercepts on the vertical axis, $q\varphi_{B0}$ is estimated to be 1.18, 1.13, and 1.16 eV for devices with different LN film thickness of 35, 49, and 88 nm, respectively.

## APPENDIX C: THE *J*-*V* CHARACTERISTICS UNDER LIGHT ILLUMINATION

Figure 10 shows the measured *J*-*V* curves under the 325-nm light illumination with various power density $P_{in}$ for three PV devices with typical LN film thickness of 16 nm [Fig. 10(a)], 42 nm [Fig. 10(b)], and 100 nm [Fig. 10(c)], respectively. Note that the corresponding $P_{in}$-dependent $|J_{sc}|$ and $V_{oc}$ for these three devices are given in Figs. 4(b) and 4(c), respectively, in the main text. We also tried to study the PV response when the spontaneous polarization $\mathbf{P}_s$ of LN crystal is reversed. However, we failed to do so because we failed to reverse completely the spontaneous polarization $\mathbf{P}_s$ of LN films, probably due to the large leakage current, which makes it a challenge to achieve a complete reversal of the spontaneous polarization $\mathbf{P}_s$. We will try to solve this polarization reversal issue in the future and study the switchability of the photovoltaic response.

## APPENDIX D: PV PERFORMANCES WITH DIFFERENT MATERIALS AND STRUCTURES

The PV performances with different materials and structures are listed in Table I for comparison.


[1] J. E. Spanier, V. M. Fridkin, A. M. Rappe, A. R. Akbashev, A. Polemi, Y. Qi, Z. Gu, S. M. Young, C. J. Hawley, D. Imbrenda *et al.*, Power conversion efficiency exceeding the Shockley–Queisser limit in a ferroelectric insulator, Nat. Photonics **10**, 611 (2016).

[2] A. G. Chynoweth, Surface space-charge layers in barium titanate, Phys. Rev. **102**, 705 (1956).

[3] V. M. Fridkin, Bulk photovoltaic effect in noncentrosymmetric crystals, Crystallogr. Rep. (Transl. Kristallografiya) **46**, 654 (2001).

[4] M. Qin, K. Yao, and Y. C. Liang, Photovoltaic mechanisms in ferroelectric thin films with the effects of the electrodes and interfaces, Appl. Phys. Lett. **95**, 022912 (2009).

[5] S. Yang, J. Seidel, S. Byrnes, P. Shafer, C.-H. Yang, M. Rossell, P. Yu, Y.-H. Chu, J. Scott, J. Ager Iii *et al.*, Above-bandgap voltages from ferroelectric photovoltaic devices, Nat. Nanotechnol. **5**, 143 (2010).

[6] Z. Tan, L. Hong, Z. Fan, J. Tian, L. Zhang, Y. Jiang, Z. Hou, D. Chen, M. Qin, M. Zeng *et al.*, Thinning ferroelectric films for high-efficiency photovoltaics based on the Schottky barrier effect, NPG Asia Mater. **11**, 20 (2019).

[7] T. Choi, S. Lee, Y. J. Choi, V. Kiryukhin, and S.-W. Cheong, Switchable ferroelectric diode and photovoltaic effect in $BiFeO_3$, Science **324**, 63 (2009).

[8] A. Bhatnagar, A. Roy Chaudhuri, Y. Heon Kim, D. Hesse, and M. Alexe, Role of domain walls in the abnormal photovoltaic effect in $BiFeO_3$, Nat. Commun. **4**, 2835 (2013).

[9] I. Grinberg, D. V. West, M. Torres, G. Gou, D. M. Stein, L. Wu, G. Chen, E. M. Gallo, A. R. Akbashev, P. K. Davies *et al.*, Perovskite oxides for visible-light-absorbing ferroelectric and photovoltaic materials, Nature **503**, 509 (2013).

[10] R. Nechache, C. Harnagea, S. Li, L. Cardenas, W. Huang, J. Chakrabartty, and F. Rosei, Bandgap tuning of multiferroic oxide solar cells, Nat. Photonics **9**, 61 (2015).

[11] R. Guo, L. You, Y. Zhou, Z. Shiuh Lim, X. Zou, L. Chen, R. Ramesh, and J. Wang, Non-volatile memory based on the ferroelectric photovoltaic effect, Nat. Commun. **4**, 1990 (2013).

[12] Y. Sun, S. Xu, Z. Xu, J. Tian, M. Bai, Z. Qi, Y. Niu, H. H. Aung, X. Xiong, J. Han *et al.*, Mesoscopic sliding ferroelectricity enabled photovoltaic random access memory for material-level artificial vision system, Nat. Commun. **13**, 5391 (2022).

[13] S. Aftab, M. Z. Iqbal, Z. Haider, M. W. Iqbal, G. Nazir, and M. A. Shehzad, Bulk photovoltaic effect in 2D materials for solar-power harvesting, Adv. Opt. Mater. **10**, 2201288 (2022).

[14] N. Ma, K. Zhang, and Y. Yang, Photovoltaic–pyroelectric coupled effect induced electricity for self-powered photodetector system, Adv. Mater. **29**, 1703694 (2017).

[15] Y. Wu, X. Wang, G. Tian, L. Zheng, F. Liang, S. Zhang, H. Yu, and H. Zhang, Inverse design of ferroelectric-order in perovskite crystal for self-powered ultraviolet photodetection, Adv. Mater. **34**, 2105108 (2022).

[16] B. Cui, Z. Fan, W. Li, Y. Chen, S. Dong, Z. Tan, S. Cheng, B. Tian, R. Tao, G. Tian *et al.*, Ferroelectric photosensor network: An advanced hardware solution to real-time machine vision, Nat. Commun. **13**, 1707 (2022).

[17] R. Weis and T. Gaylord, Lithium niobate: Summary of physical properties and crystal structure, Appl. Phys. A **37**, 191 (1985).

[18] I. Shoji, T. Kondo, A. Kitamoto, M. Shirane, and R. Ito, Absolute scale of second-order nonlinear-optical coefficients, J. Opt. Soc. Am. B **14**, 2268 (1997).

[19] E. Turner, High-frequency electro-optic coefficients of lithium niobate, Appl. Phys. Lett. **8**, 303 (1966).

[20] F. Chen, Optically induced change of refractive indices in $LiNbO_3$ and $LiTaO_3$, J. Appl. Phys. **40**, 3389 (1969).

[21] A. Glass, D. von der Linde, and T. Negran, High-voltage bulk photovoltaic effect and the photorefractive process in $LiNbO_3$, Appl. Phys. Lett. **25**, 233 (1974).

[22] H. Festl, P. Hertel, E. Krätzig, and R. v. Baltz, Investigations of the photovoltaic tensor in doped $LiNbO_3$, Phys. Status Solidi B **113**, 157 (1982).

[23] F. Xin, Z. Zhai, X. Wang, Y. Kong, J. Xu, and G. Zhang, Threshold behavior of the einstein oscillator, electron-phonon interaction, band-edge absorption, and small hole polarons in $LiNbO_3$:Mg crystals, Phys. Rev. B **86**, 165132 (2012).

[24] R. Inoue, S. Takahashi, Y. Kitanaka, T. Oguchi, Y. Noguchi, and M. Miyayama, Enhanced photovoltaic currents in strained Fe-doped $LiNbO_3$ films, Phys. Status Solidi A **212**, 2968 (2015).

[25] J. Wang, X. Pan, Q. Wang, W. Luo, Y. Shuai, Q. Xie, H. Zeng, G. Niu, C. Wu, and W. Zhang, Reliable resistive switching and synaptic plasticity in $Ar^+$-irradiated single-crystalline $LiNbO_3$ memristor, Appl. Surf. Sci. **596**, 153653 (2022).

[26] J. P. McConville, H. Lu, B. Wang, Y. Tan, C. Cochard, M. Conroy, K. Moore, A. Harvey, U. Bangert, L.-Q. Chen *et al.*, Ferroelectric domain wall memristor, Adv. Funct. Mater. **30**, 2000109 (2020).

[27] Y. Qian, Y. Zhang, J. Xu, and G. Zhang, Domain-wall *p-n* junction in lithium niobate thin film on an insulator, Phys. Rev. Appl. **17**, 044011 (2022).

[28] G. Clementi, G. Lombardi, S. Margueron, M. A. Suarez, E. Lebrasseur, S. Ballandras, J. Imbaud, F. Lardet-Vieudrin, L. Gauthier-Manuel, B. Dulmet *et al.*, $LiNbO_3$ films–a low-cost alternative lead-free piezoelectric material for vibrational energy harvesters, Mech. Syst. Signal Proc. **149**, 107171 (2021).

[29] H. Guan, J. Hong, X. Wang, J. Ming, Z. Zhang, A. Liang, X. Han, J. Dong, W. Qiu, Z. Chen, H. Lu, and H. Zhang, Broadband, high-sensitivity graphene photodetector based on ferroelectric polarization of lithium niobate, Adv. Opt. Mater. **9**, 2100245 (2021).

[30] X. Sun, Y. Sheng, X. Gao, Y. Liu, F. Ren, Y. Tan, Z. Yang, Y. Jia, and F. Chen, Self-powered lithium niobate thin-film photodetectors, Small **18**, 2203532 (2022).

[31] R. Jungen, G. Angelow, F. Laeri, and C. Grabmaier, Efficient ultraviolet photorefraction in $LiNbO_3$, Appl. Phys. A **55**, 101 (1992).

[32] A. Abdelsamie, L. You, L. Wang, S. Li, M. Gu, and J. Wang, Crossover between bulk and interface photovoltaic mechanisms in a ferroelectric vertical heterostructure, Phys. Rev. Appl. **17**, 024047 (2022).

[33] W.-C. Yang, B. J. Rodriguez, A. Gruverman, and R. Nemanich, Polarization-dependent electron affinity of $LiNbO_3$ surfaces, Appl. Phys. Lett. **85**, 2316 (2004).

[34] D. E. Eastman, Photoelectric work functions of transition, rare-earth, and noble metals, Phys. Rev. B **2**, 1 (1970).

[35] S. M. Sze and K. K. Ng, *Physics of Semiconductor Devices* (John Wiley & Sons, Ltd, Hoboken, 2006).

[36] M. Dawber, K. M. Rabe, and J. F. Scott, Physics of thin-film ferroelectric oxides, Rev. Mod. Phys. **77**, 1083 (2005).

[37] B. S. Eller, J. Yang, and R. J. Nemanich, Electronic surface and dielectric interface states on GaN and AlGaN, J. Vac. Sci. Technol. A **31**, 050807 (2013).

[38] L. Pintilie and M. Alexe, Metal-ferroelectric-metal heterostructures with Schottky contacts. I. Influence of the ferroelectric properties, J. Appl. Phys. **98**, 124103 (2005).

[39] L. You, A. Abdelsamie, Y. Zhou, L. Chang, Z. S. Lim, and J. Wang, Revisiting the ferroelectric photovoltaic properties of vertical $BiFeO_3$ capacitors: A comprehensive study, ACS Appl. Mater. Interfaces **15**, 12070 (2023).

[40] H. Han, D. Kim, S. Chae, J. Park, S. Y. Nam, M. Choi, K. Yong, H. J. Kim, J. Son, and H. M. Jang, Switchable ferroelectric photovoltaic effects in epitaxial *h*-$RFeO_3$ thin films, Nanoscale **10**, 13261 (2018).

[41] D. Cao, Z. Wang, Nasori, L. Wen, Y. Mi, and Y. Lei, Switchable charge-transfer in the photoelectrochemical energy-conversion process of ferroelectric $BiFeO_3$ photoelectrodes, Angew. Chem. **126**, 11207 (2014).

[42] F. Zheng, J. Xu, L. Fang, M. Shen, and X. Wu, Separation of the Schottky barrier and polarization effects on the photocurrent of Pt sandwiched $Pb(Zr_{0.20}Ti_{0.80})O_3$ films, Appl. Phys. Lett. **93**, 172101 (2008).

[43] R. L. Gao, H. W. Yang, Y. S. Chen, J. R. Sun, Y. G. Zhao, and B. G. Shen, Oxygen vacancies induced switchable and nonswitchable photovoltaic effects in $Ag/Bi_{0.9}La_{0.1}FeO_3/La_{0.7}Sr_{0.3}MnO_3$ sandwiched capacitors, Appl. Phys. Lett. **104**, 031906 (2014).

[44] O. F. Schirmer, Q. Thiemann, and M. Wöhlecke, Defects in $LiNbO_3$–I. Experimental aspects, J. Phys. Chem. Solids **52**, 185 (1991).

[45] Y. Sun and R. J. Nemanich, Photoinduced Ag deposition on periodically poled lithium niobate: Wavelength and polarization screening dependence, J. Appl. Phys. **109**, 104302 (2011).

[46] L. Pintilie, I. Vrejoiu, D. Hesse, G. LeRhun, and M. Alexe, Ferroelectric polarization-leakage current relation in high quality epitaxial $Pb(Zr, Ti)O_3$ films, Phys. Rev. B **75**, 104103 (2007).

[47] J. Gao, J. M. Luther, O. E. Semonin, R. J. Ellingson, A. J. Nozik, and M. C. Beard, Quantum dot size dependent *J-V* characteristics in heterojunction ZnO/PbS quantum dot solar cells, Nano Lett. **11**, 1002 (2011).

[48] S. Yoo, B. Domercq, and B. Kippelen, Intensity-dependent equivalent circuit parameters of organic solar cells based on pentacene and $C_{60}$, J. Appl. Phys. **97**, 103706 (2005).

[49] A. Jain and A. Kapoor, Exact analytical solutions of the parameters of real solar cells using Lambert *W*-function, Sol. Energy Mater Sol. Cells **81**, 269 (2004).

[50] R. Zhuo, L. Zeng, H. Yuan, D. Wu, Y. Wang, Z. Shi, T. Xu, Y. Tian, X. Li, and Y. H. Tsang, *In-situ* fabrication of $PtSe_2/GaN$ heterojunction for self-powered deep ultraviolet photodetector with ultrahigh current on/off ratio and detectivity, Nano Res. **12**, 183 (2019).

[51] H. Kind, H. Yan, B. Messer, M. Law, and P. Yang, Nanowire ultraviolet photodetectors and optical switches, Adv. Mater. **14**, 158 (2002).

[52] P. P. Biswas, S. Pal, V. Subramanian, and P. Murugavel, Polarization driven self-biased and enhanced UV-visible photodetector characteristics of ferroelectric thin film, J. Phys. D: Appl. Phys. **53**, 275302 (2020).

[53] S. Zeiske, W. Li, P. Meredith, A. Armin, and O. J. Sandberg, Light intensity dependence of the photocurrent in organic photovoltaic devices, Cell Rep. Phys. Sci. **3**, 101096 (2022).

[54] Y. J. Zhang, T. Ideue, M. Onga, F. Qin, R. Suzuki, A. Zak, R. Tenne, J. H. Smet, and Y. Iwasa, Enhanced intrinsic photovoltaic effect in tungsten disulfide nanotubes, Nature **570**, 349 (2019).

[55] H. Liu, J. Chen, Y. Ren, L. Zhang, Z. Pan, L. Fan, and X. Xing, Large photovoltage and controllable photovoltaic effect in $PbTiO_3$-$Bi(Ni_{2/3+x}Nb_{1/3-x})O_{3-\delta}$ ferroelectrics, Adv. Electron. Mater. **1**, 1400051 (2015).

[56] S. Nandy, K. Kaur, S. Gautam, K. H. Chae, B. Nanda, and C. Sudakar, Maximizing short circuit current density and open circuit voltage in oxygen vacancy-controlled $Bi_{1-x}Ca_xFe_{1-y}Ti_yO_{3-\delta}$ thin-film solar cells, ACS Appl. Mater. Interfaces **12**, 14105 (2020).

[57] D. Feng, B. Huang, L. Li, X. Li, Y. Gu, W. Hu, and Z. Zhang, The effects of $Eu^{3+}$ doping on the epitaxial growth and photovoltaic properties of $BiFeO_3$ thin films, J. Mater. Sci. Technol. **106**, 49 (2022).

[58] D. Cao, C. Wang, F. Zheng, W. Dong, L. Fang, and M. Shen, High-efficiency ferroelectric-film solar cells with an n-type $Cu_2O$ cathode buffer layer, Nano Lett. **12**, 2803 (2012).

[59] J.-M. Yan, K. Wang, Z.-X. Xu, J.-S. Ying, T.-W. Chen, G.-L. Yuan, T. Zhang, H.-W. Zheng, Y. Chai, and R.-K. Zheng, Large ferroelectric-polarization-modulated photovoltaic effects in bismuth layered multiferroic/semiconductor heterostructure devices, J. Mater. Chem. C **9**, 3287 (2021).

[60] H. Renuka, A. Garudapalli, T. A. Raman, B. H. Venkataraman, K. Ramaswamy, K. James Raju, S. Goel, and S. Kundu, Enhanced photovoltaic response in ferroelectric Ti-doped BFO heterojunction through interface engineering for building integrated applications, Sol. Energy **225**, 863 (2021).

[61] A. Zenkevich, Y. Matveyev, K. Maksimova, R. Gaynutdinov, A. Tolstikhina, and V. Fridkin, Giant bulk photovoltaic effect in thin ferroelectric $BaTiO_3$ films, Phys. Rev. B **90**, 161409 (2014).

[62] Z. Gu, D. Imbrenda, A. L. Bennett-Jackson, M. Falmbigl, A. Podpirka, T. C. Parker, D. Shreiber, M. P. Ivill, V. M. Fridkin, and J. E. Spanier, Mesoscopic free path of nonthermalized photogenerated carriers in a ferroelectric insulator, Phys. Rev. Lett. **118**, 096601 (2017).

[63] F. Zheng, P. Zhang, X. Wang, W. Huang, J. Zhang, M. Shen, W. Dong, L. Fang, Y. Bai, X. Shen, H. Sun, and J. Hao, Photovoltaic enhancement due to surface-plasmon assisted visible-light absorption at the inartificial surface of lead zirconate-titanate film, Nanoscale **6**, 2915 (2014).

[64] J. G. Simmons, Generalized formula for the electric tunnel effect between similar electrodes separated by a thin insulating film, J. Appl. Phys. **34**, 1793 (1963).

[65] J. G. Simmons, Electric tunnel effect between dissimilar electrodes separated by a thin insulating film, J. Appl. Phys. **34**, 2581 (1963).

[66] W. F. Brinkman, R. C. Dynes, and J. M. Rowell, Tunneling conductance of asymmetrical barriers, J. Appl. Phys. **41**, 1915 (1970).

[67] D. Pantel, H. Lu, S. Goetze, P. Werner, D. J. Kim, A. Gruverman, D. Hesse, and M. Alexe, Tunnel electroresistance in junctions with ultrathin ferroelectric $Pb(Zr_{0.2}Ti_{0.8})O_3$ barriers, Appl. Phys. Lett. **100**, 232902 (2012).

[68] S. Nakashima, R. Kato, and H. Fujisawa, Impact of flim thickness on the external quantum efficiency of bulk photovoltaic effects in Mn-doped $BiFeO_3$ thin films, Jpn. J. Appl. Phys. **60**, SFFB02 (2021).

[69] Y. Li, J. Fu, X. Mao, C. Chen, H. Liu, M. Gong, and H. Zeng, Enhanced bulk photovoltaic effect in two-dimensional ferroelectric $CuInP_2S_6$, Nat. Commun. **12**, 5896 (2021).